ELSEVIER

Contents lists available at ScienceDirect

Ultramicroscopy

journal homepage: www.elsevier.com/locate/ultramic



Design and application of a relativistic Kramers-Kronig analysis algorithm

Alberto Eljarrat*, Christoph T. Koch

Department of Physics, Humboldt University of Berlin, Newtonstraße 15, Berlin 12489, Germany



ARTICLE INFO

Keywords: EELS Kramers-Kronig analysis Opto-electronic properties

ABSTRACT

Low-loss electron energy loss spectroscopy (EELS) in the scanning transmission electron microscope probes the valence electron density and relevant optoelectronic properties such as band gap energies and other band structure transitions. The measured spectra can be formulated in a dielectric theory framework, comparable to optical spectroscopies and ab-initio simulations. Moreover, Kramers–Kronig analysis (KKA), an inverse algorithm based on the same name relations, can be employed for the retrieval of the complex dielectric function. However, spurious contributions traditionally not considered in this framework typically impact low-loss EELS modifying the spectral shapes and precluding the correct measurement and retrieval of the dielectric information. A relativistic KKA algorithm is able to account for the bulk and surface radiative-loss contributions to low-loss EELS, revealing the correct dielectric properties. Using a synthetic low-loss EELS model, we propose some modifications on the naive implementation of this algorithm that broadens its range of application. The robustness of the algorithm is improved by regularization, applying previous knowledge about the shape and smoothness of the correction term. Additionally, our efficient numerical integration methodology allows processing hyperspectral datasets in a reasonable amount of time. Harnessing these abilities, we show how simultaneous relativistic KKA processing of several spectra can share information to produce an improved result.

1. Introduction

Low-loss electron energy loss spectroscopy (EELS) in the scanning transmission electron microscope (STEM) combines the ability to measure dielectric properties with ultimate spatial resolution. This ability complements other experimental and theoretical techniques being applied in the characterization of the optoelectronic properties of materials. For instance, ab-initio simulation codes based on density functional theory (DFT) are able to calculate related quantities with varying degrees of precision [1–3]. Moreover, optical spectroscopy techniques measure spatial averages of some of the (optical) transitions observed in EELS [4]. Generally speaking, the theoretical framework in which these techniques are formulated has one relevant quantity in common; a complex dielectric function (CDF), that describes the displacement of bound charges in the material when exposed to exterior electric fields. Being able to measure or calculate this quantity is relevant in many fields, for instance to the characterization of semiconductor materials [5,6]. In this sense, a long standing aim has been to use low-loss EELS to perform standard-free measurement of the dielectric properties of materials ranging from the optical to the ultraviolet (UV) frequency regime, without having to revert to synchrotron radiation [7-9].

The study of the dielectric response in low-loss EELS is characterized by the choice of a semi-classical or relativistic framework. In the semi-classical formulation, closed formulas describe the energy-loss spectrum in terms of the CDF [10]. Together with the causality properties of the dielectric response, this formulation has traditionally been used in the Kramers–Kronig analysis (KKA) to retrieve the CDF [5,9,11]. In most cases a relativistic framework has to be considered to completely describe the low-loss EELS signal, as pointed out in early theoretical and experimental work [7,12,13]. Bulk and surface radiative-loss modes are only explained in this relativistic formulation. It is possible that the generally poor energy resolution of conventional transmission electron microscopes (TEMs) equipped for EELS made the study of these modes less relevant and prioritized surface-losses that impact the spectra at a higher energy-loss range.

The interest in the relativistic formulation increased with the general availability of sub-eV resolution in STEM-EELS. Relevant (opto-) electronic properties, such as the band gap energy in semiconductor materials, can in principle be measured by modern low-loss EELS systems [5,14]. However, under common experimental conditions, spectral features indicating the band gap energy onset may be concealed by bulk radiative loss contributions (i.e. Cerenkov-losses) [15], making the interpretation of the data problematic. Some experimental methods

E-mail addresses: aeljarrat@physik.hu-berlin.de, aeljarrat@el.ub.edu (A. Eljarrat).

^{*} Corresponding author.

have been proposed to circumvent or reduce the impact of these spurious contributions and allow the direct observation of the band gap. Among these, using lower electron beam energies and thinner samples can help in the overall reduction of the intensity of bulk radiative losses [16]. Other experimental methods attempt to suppress this contribution by avoiding the forward scattered electrons, either by using a dedicated experimental setup [17,18,18–20]; or by subtracting spectra acquired with different collection apertures [21].

Since these methods do not guarantee a complete correction of the relativistic and surface effects and are not always feasible, off-line analysis methods must be considered as well. Their theoretical framework should include the relativistic (bulk and surface) contributions to low-loss EELS, and provide a way to extract the underlying material dependent spectral features from the experimental data. It is, in principle, possible to introduce a calculation of the relativistic double differential cross section (DDCS) into the KKA framework in order to calculate such off-line correction [19]. In the classical KKA framework, the analytically integrable semi-classical DDCS model is used; producing a closed expression for the surface correction. Conversely, the relativistic DDCS has to be integrated over a mesh of scattering angles using numerical methods. The computations involved are more costly and, as shown below, there are several pitfalls in this process. Some authors have proposed methods to deal with these issues, e.g. by using simple models of the CDF in Silicon [22], or more recently by proposing more sophisticated integration methods for the relativistic DDCS [23].

Our study of this problem begins by describing a framework for the simulation of realistic low-loss EELS synthetic data, using an analytical model for the dielectric function of a material characterized by a band gap and bulk plasmon. This model is useful also to study the forward simulation of spectra from dielectric data, which is an integral part of the KKA algorithm.

This study is the basis of our implementation of the relativistic KKA (rKKA) algorithm, that is designed with reliability and speed in mind. In our version of this algorithm, the iteratively-updated relativistic correction term is obtained using a single-step numerical integration of a special relativistic DDCS. Since this computation is costly and not free of errors, several numerical integration methods are implemented in our algorithm and a comparison in terms of their cost and performance is made. Additionally, parallel computation improves the processing time for hyperspectral datasets.

Some instabilities and artifacts affecting the results obtained from the rKKA algorithm are found. Our tests show that these issues are mostly related to the inaccuracy of the initial guess for the dielectric function and the response of the algorithm to noise in the input spectra. The robustness of our rKKA algorithm against this issues is improved by implementing a simple regularization scheme of the correction term by bounding and smoothing.

Finally, a novel methodology is proposed, that integrates the information from the analysis of hyperspectral datasets in which several spectra from the same material are included. In a first proof-of-concept, we show that the estimate of the CDF made at different thicknesses can be averaged, further improving the robustness of the rKKA algorithm.

The software developed for this work is implemented in Python using the Hyperspy toolbox [24], and can be obtained on github [25]. The use of fast numerical integration methods and parallel computing makes it generally useful for the simulation and rKKA of EELS spectra. The rKKA has been tested both on synthetic and experimental data (experimental results are presented in a different paper).

2. Materials and methods

2.1. Dielectric response model

For linear continuous media, the low-loss EELS signal from a thinfilm sample is completely described by the dielectric tensor, $\varepsilon = \varepsilon_{ij}(\mathbf{q}, E)$; where \mathbf{q} is the scattering vector and E is the energy-loss; and a few experiment-dependent parameters [9]. From a macroscopic point of view, this is a complex tensor describing polarization of the material in response to an external electric field. For a microscopic description of the polarization induced by the electron beam, one has to consider a model of the applied perturbation and the bound charge density together with some approximations. Let us consider the special case of small-angle scattering, dictated by the (longitudinal) Coulomb force and Bloch wave-functions in isotropic media. In this case, the ${\bf q}$ dependence and the tensor nature are dropped and the dielectric response is completely described by the CDF, $\varepsilon = \varepsilon(E)$.

This formalism is equivalent to applying the random-phase approximation (RPA), that is employed in DFT to simulate dielectric properties; or to the Lindhard model [26], at the core of many CDF models used to fit optical signals. It is an independent particle approximation and in consequence, many-body effects such as spin exchange or Coulomb correlation are not included. However, this simple description is sufficient for the current work, which aims at providing phenomenological insight into the behavior of low-loss EELS in terms of optical transitions in the presence of relativistic effects.

In this framework, a dielectric response model that is useful for the simulation and KKA of low-loss EELS can be obtained considering the electric susceptibility, $\chi = \varepsilon - 1$. This quantity can be theoretically obtained by the product of appropriate transition matrix elements and the valence joint density of states (JDOS) [11]. Such models of the susceptibility are useful since this quantity is additive and directly related to the imaginary part of the CDF [9]. In other words, the imaginary part of the CDF can be described as the sum of individual susceptibilities, χ_j , for each separate contribution. The real part can be obtained from the imaginary part using the appropriate Kramers–Kronig transformation (KKT);

$$\varepsilon = 1 + \text{KKT}[\Im(\varepsilon)] + i\Im(\varepsilon); \ \Im(\varepsilon) = \sum \chi_j$$
 (1)

For many materials, the main contributions to low-loss spectra come from single electron transitions and plasmon excitations. Among the former, the band gap energy onset is perhaps the most relevant feature in semiconductor and dielectric materials. To model a semiconductor featuring a direct band gap transition, the Tauc JDOS model is a natural choice for the imaginary part of the susceptibility [4],

$$\Im(\chi_T) = \frac{f_g^2 \sqrt{E - E_g}}{E^2} H(E - E_g)$$
 (2)

Where E_g is the band gap energy, f_g is proportional to the transition oscillator strength and H is the Heaviside step function. For the plasma oscillation, perhaps the simplest model is a Lorenz oscillator. A hybrid Tauc–Lorenz (TL) model is used in the analysis of ellipsometric data [27], in order to account for the shift of the plasmon resonance induced by the band gap transition,

$$\Im(\chi_{TL}) = \frac{f_P^2}{E} \frac{E_P \Gamma_P (E - E_g)^2}{(E^2 - E_P^2)^2 + E^2 \Gamma^2} H(E - E_g)$$
(3)

Where E_P is the plasmon energy, Γ_P is the plasmon width, and f_P is again the resonance strength. The dielectric function model used in the present work is obtained by adding the two susceptibilities presented above; $\Im(\varepsilon_{TL}) = \chi_T + \chi_{TL}$. Fig. 1a portraits these models for $E_g = 1$, 3 and 5 eV, in gray-filled areas. Additionally, the absorption is null below the band gap and the absorption decays with an inverse cubic dependence or faster for large energy-losses.

Note that the full complex ε_{TL} (not shown in the figure) is needed for the dielectric model of EELS simulations; this is obtained using Eq. 1. Because of this formulation, the ε_{TL} model agrees perfectly with the Kramers–Kronig relations, which constitute the basic property that enables the KKA. We confirm this fact by transforming back and forth the real and imaginary parts of the ε_{TL} models, and also simulating semi-classical low-loss EELS spectra and processing them via the KKA. In both cases, the original and retrieved dielectric functions agree,

indicating that the Kramers-Kronig relations hold for ε_{TL} .

A word of caution: our tests using analytical models for the CDF, e.g. the Drude model [9], showed that for some parameters small discrepancies between the analytically calculated real and imaginary parts and their respective KKT can appear. In these tests, the KKT was implemented both in reciprocal and real space using FFT and MacLaurin method, respectively. Although small, these discrepancies are somehow transferred to the calculated spectra even if a broad energy range is considered. In those cases verifying the validity of KKA is hampered by the fact that agreement between the original and recovered CDF is not guaranteed. Using Eq. 1 to generate a CDF model that agrees with KKT from only the imaginary part is also a solution to this issue.

2.2. Dielectric formulation of EELS

Single scattering distribution (SSD) energy-loss spectra, S(E), can be calculated from the different ε_{TL} models (see for instance Fig. 1). Disregarding plural scattering, these S(E) emulate experimentally obtained low-loss EELS for thin samples. These calculations are performed using a formulation of EELS that links dielectric theory and the observed low-loss spectra. This dielectric formulation of EELS is based on Maxwell's equations, solved for the charge distribution in the bulk and at the boundaries of the object. Since the potential can generally be separated into bulk and boundary reflection terms, we obtain separate expressions for the bulk and surface DDCS [28]. The total spectrum can be found by integrating these DDCS and adding each contribution, $S = S_b + S_s$;

$$S_{b,s}(E) = \int_0^{\theta_{max}} D_{b,s}(\theta, E) \sin(\theta) d\theta$$
 (4

Where $D_{b,s}$ and $S_{b,s}$ are the bulk and surface DDCS and energy-loss spectra, respectively; and θ is the scattering angle. For both bulk and surface modes, depending if retardation effects are considered in the DDCS models, semi-classical and relativistic contributions to the total spectrum can be identified.

For the semi-classical case retardation effects are disregarded and analytical integration of the DDCS is possible [10]. Then, closed formulas that model S(E) as a function of $\varepsilon(E)$ can be obtained, taking into account only a few parameters; the incoming beam energy, E_0 ; the transversed material thickness, t; and the scattering angle cut-off, $\theta_{\rm max}$. In this formulation the bulk term is proportional to the inverse of the dielectric function multiplied by a known angular integration term,

$$S_b^{ELF}(E) = \frac{2I_0 t \Im(-1/\varepsilon)}{\pi^2 a_0 m_0 v^2} \ln[1 + (\theta_{max}/\theta_E)^2]$$
(5)

Where I_0 is the zero-loss intensity, a_0 is the Bohr radius, m_0 is the electron rest mass, ν is the electron speed and $\theta_E = E/(\gamma m_0 \nu^2)$ is the characteristic scattering angle. Moreover, $\Im(-1/\varepsilon)$ is also called the energy-loss function (ELF). This ELF produces a contribution that has a fixed shape given by Eq. 5 and scales linearly with thickness. For samples with thickness above a few tens of nm this contribution always dominates S(E). Examples can be found in Fig. 1, where the spectra in panel (b) correspond to $\Im(-1/\varepsilon_{TL})$.

However, a mostly thickness independent surface-loss term from the sample boundaries always exists. A closed-form expression can be provided for this term but will not be reproduced here, the reader is referred elsewhere [11]. The surface contribution modifies the spectral shape, mainly by adding an additional surface-plasmon peak that can be observed and sometimes dominates in very thin specimens. Additionally, $S_s(E)$ features a region of negative intensity, representing a reduction of the EELS signal.

A fully relativistic description (i.e. including retardation effects) has to be considered when the speed of the fast electrons surpasses the phase velocity of light in the medium $\Re(\epsilon) > c^2/v^2$. This is a common case for the analysis of materials in the STEM, because of the high kinetic energy of the electron beam of typically 200 or 300 keV. In those cases, including retardation effects into the DDCS produces a more

intricate model with additional contributions [12],

$$D(\theta, E) = D_b + D_s = \frac{l_0}{\pi^2 a_0 m_0 v^2} \Im \left[\frac{\iota \mu^2}{\epsilon^* \varphi^2} - \frac{2\theta^2 (\epsilon^* - \eta^*)^2}{k_0 \varphi_0^4 \varphi^4} (A + B + C) \right]$$
(6)

Where $\varepsilon^* = \varepsilon_1 - i\varepsilon_2$ is the complex conjugate of the dielectric function for the specimen, and η^* , idem for the surroundings (in this work, $\eta^* = 1$ for vacuum). Moreover, μ and ϕ are dimensionless quantities related to momentum exchange and the A, B, and C are terms representing different surface-loss terms, by surface-plasmon and guidedlight modes. To avoid cluttering, the relatively intricate dependence of these terms on θ , E and t is not described here, their definitions can be found elsewhere [9], and also the original derivations [12,13].

This complexity poses a challenge to analytically solve Eq. 4, and to our knowledge there are no available closed formulas for S(E) in the relativistic formulation. Nevertheless, the relativistic DDCS can be integrated numerically (more below). For thin samples and comparing to the semi-classical formulation, once the retardation effects are taken into account this means a radical modification of the bulk and surface terms, despite a similar dependence on specimen thickness. Bulk radiative-loss excitation is now possible, emitting Cerenkov radiation with an intensity directly proportional to the thickness. Additionally, a variety of boundary coupling effects are observed depending on the interfaces and surfaces of the material.

Figs. 1 b and 2 a illustrate the importance of bulk and surface, the semi-classical model and contributions due to relativistic effects. In these panels, the featured S(E) are calculated using the numerically integrated full relativistic model of Eq. 6 (solid black lines) and compared to the contribution of the bulk semi-relativistic term described by Eq. 5 (in grey areas). The latter is clearly dominant, however S(E) departs from the shape dictated by $\Im(-1/\varepsilon_{TL})$ by an the additional peak appearing around the [13.5, 14.0] eV energy region, which is the due to the surface contribution. Mind that according to Eq. 6, surface contributions are calculated separately showing a surface plasmon peak at this approximate energy-loss for our ε_{TL} models. Additionally, the spectral shape in the lower energy-loss range, close to the band gap energy onset, is radically modified; this time by Cerenkov loss. Finally, note that a Poisson-distributed random contribution has been added to these spectra to simulate the effect of noise accompanying the detection process.

The relativistic DDCS corresponding to these spectra are also depicted in Fig. 2b. Advanced, numerical integration is employed to simulate relativistic spectra, making the calculations much more demanding than for the semi-classical model. For this task, a DDCS mesh with one entry for each pair of scattering angle and energy loss values is used. From these, a numerical integration routine of choice estimates the angle-integrated SSD. For the relativistic DDCS, the use of a logarithmic mesh (log-mesh) of angles is customary, since accounting for small-angle variations with a linear mesh would require a huge number of entries. The reasons for this are visible in Fig. 2b: the radiative loss modes appear mainly at very small scattering angles ($\theta \sim \mu rad$), all the while, the spectra are usually acquired with relatively large cut-off angles ($\theta_{max} \sim mrad$), to increase counting statistics.

Numerical integration of the DDCS constitutes a slow and errorprone process, which in this work we aim to optimize. The main reason for this is that simple numerical integration algorithms are not useful to integrate the DDCS which is ideally specified on an irregularly-spaced angular log-mesh, and more sophisticated methods have to be applied. We have performed benchmark tests of integration methods, as illustrated in Fig. 2a, the outcomes of which will be discussed in Section 3.1.

2.3. Kramers-Kronig analysis

The KKA algorithm solves the inverse problem of extracting the

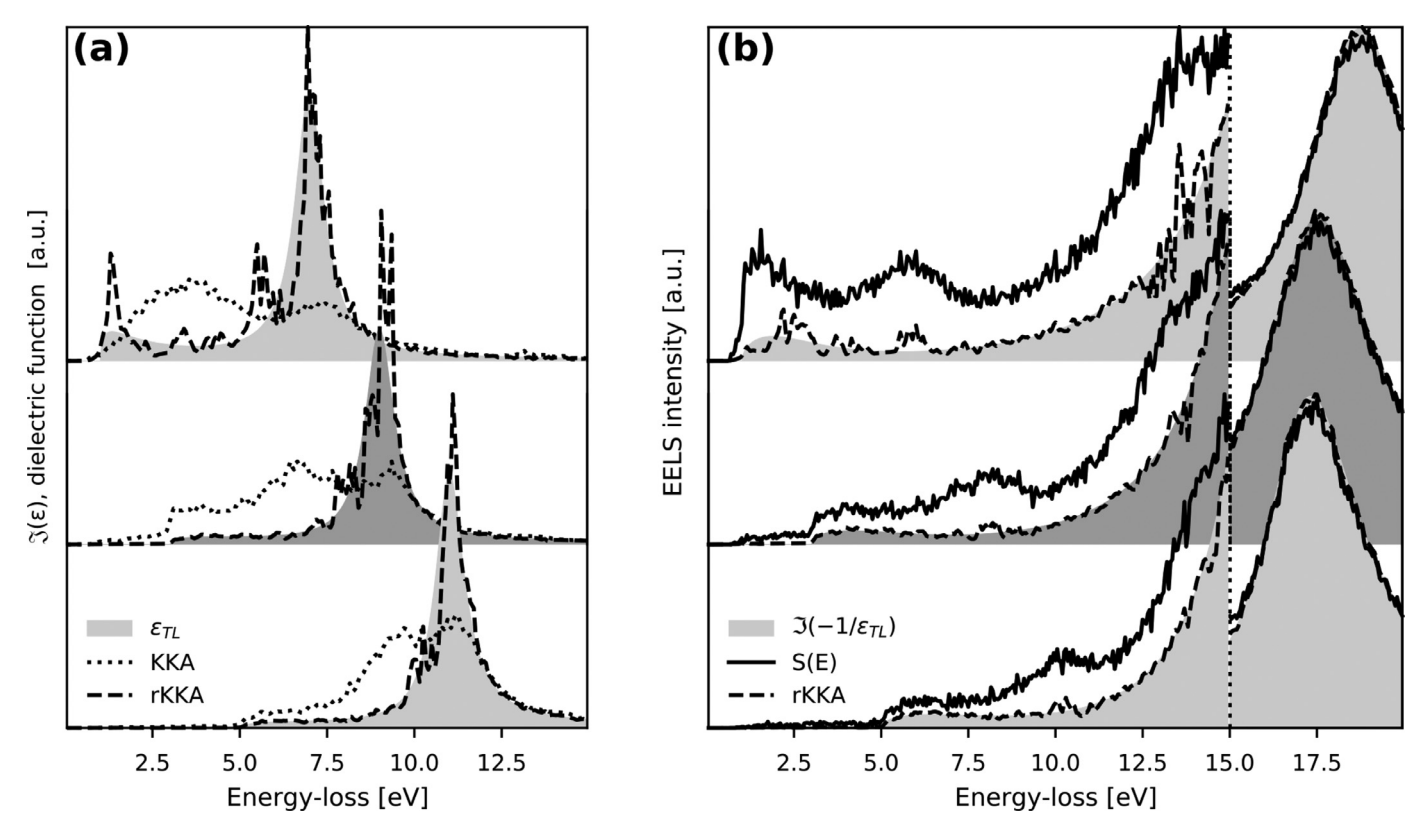


Fig. 1. Comparison of the $ε_{TL}$ model simulations and the results obtained by traditional and relativistic KKA, for t = 50 nm and $E_g = 1, 3, 5$ eV, from top to bottom. Panel (a) shows the imaginary part of the models (grey areas) compared to the KKA and rKKA reconstructions (finely dotted and dashed lines, respectively). Panel (b) shows the $\Im(-1/ε)$ contribution (grey areas) and the relativistic spectra (solid lines) calculated for these models. A dashed line shows the estimated $\Im(-1/ε)$ contribution, after rKKA correction S_c is applied. Details of the simulation and analysis parameters are found in the text.

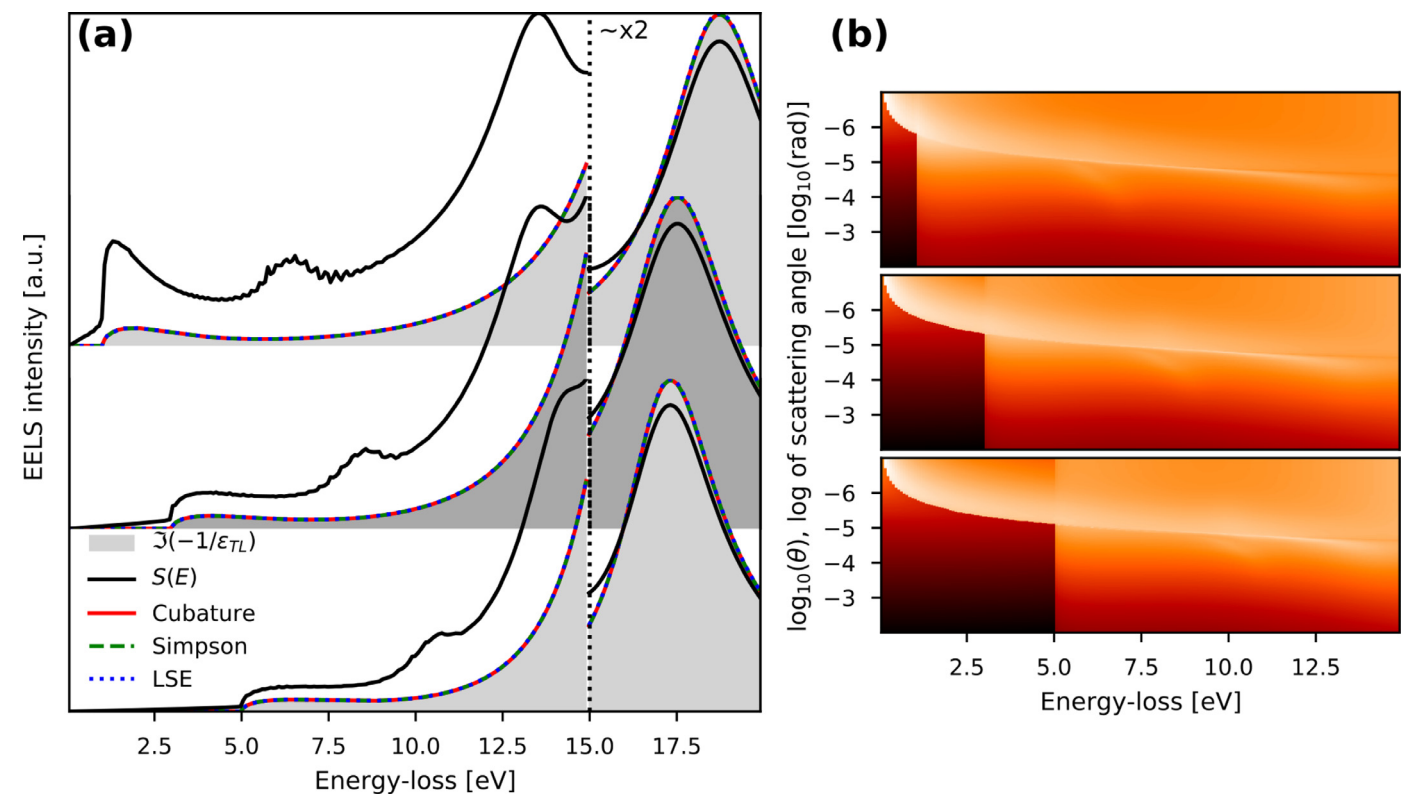


Fig. 2. For the same three ε_{TL} models presented in Fig. 1, panel (a) is showing simulated relativistic spectra (solid lines) while their corresponding DDCS log-mesh can be found in panel (b). Panel (a) also compares the analytical $\Im(-1/\varepsilon)$ contribution to the numerical estimation obtained using cubature, the Simpson-rule and LSE trick methods.

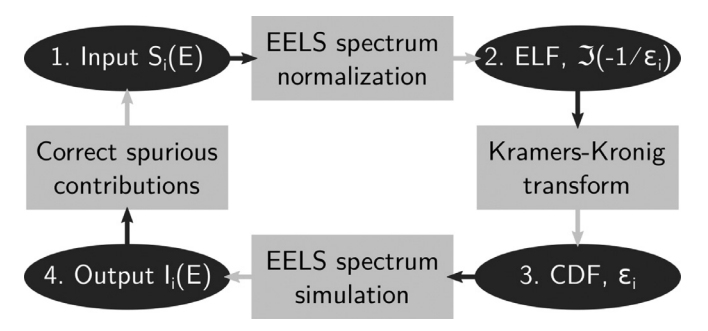


Fig. 3. Diagram showing the individual processing steps of the KKA; starting from the normalization of the spectrum to obtain an estimate of the ELF; the Kramers–Kronig transformation to retrieve the CDF; and simulation of the underlying model to correct the spurious (surface) contributions.

dielectric response of a material from experimental EELS measurements of a specimen with finite thickness. In its original formulation, KKA uses the expressions of the semi-classical dielectric formulation to relate the measurements to the ELF. Additionally, surface-loss contributions are estimated and suppressed. This process is commonly implemented as an iterative algorithm with 4 main steps, as depicted in the diagram in Fig. 3. These steps are explained below, without going into unnecessary detail. The basis of this method is also explained at length and including some application examples elsewhere [9,11].

As explained above, in the semi-classical approximation $\Im(-1/\varepsilon)$ can be obtained from normalization of S_b , the main contribution to S(E). In order to obtain the normalization factor, knowledge of the sample thickness is necessary. In cases where this parameter is not accurately known (i.e. in most experiments), the Kramers–Kronig sum-rule can be used to obtain an estimate of the thickness. After normalization the full dielectric function is obtained by application of the Kramers–Kronig transform, $\Re(1/\varepsilon) = 1 - \text{KKT}[\Im(-1/\varepsilon)]$, and some simple algebra. Using fast Fourier transform (FFT), this transform can be implemented fast and reliably in the time-domain if the EELS intensity at high energy-loss decays smoothly [29]. Using this procedure at each iteration, i, and for each input spectrum S_b , a dielectric function, ε_i is estimated.

Having reached this point (item 3 in Fig. 3), it is important to note that even if the normalization factor is perfectly known the resulting estimate of the ELF contains spurious contributions. In the semi-classical model, these stem from the ignored surface-loss term. Moreover, the dielectric function retrieved after applying the Kramers–Kronig transform is in principle also affected by these contributions. Consequently, the last two steps of the KKA loop aim at measuring the spurious contributions present in the original input signal, in order to suppress them from the estimate of S_b . Since the KKA is formulated in a non-relativistic framework, this contribution is limited to S_s .

 S_s is estimated from the current guess of the CDF, ε_i , and using the same parameters that were assumed for the normalization step. At each iteration i the surface contribution, $S_{s,i}$ of the underlying model of the signal, $I_i(E) = S_{b,i} + S_{s,i}$ is thus computed.

At the end of each iteration, the current estimate $S_{s,i}$ is applied as a correction to the original input spectrum, updating the input $S_{i+1}(E)$ used for the next iteration. For obvious reasons, this correction term is termed surface-plasmon estimation. Traditional KKA is fast and reliable, and usually converges after a few iterations [9]. A calculation can be considered converged either when the underlying model and the original spectrum are equal, i.e. when $I_i(E) \simeq S(E)$; or, alternatively, when the correction does not change any more between iterations, i.e. when $S_{s,i} \simeq S_{s,i-1}$.

However, traditional KKA neglects relativistic terms and does not perform well when these are included in the input S(E). However, these contributions are present in real EELS spectra, and the CDF retrieved from the application of KKA to these are known to contain errors [15,18]. Some example results from the application of KKA to

relativistic spectra can be examined in Fig. 1a, with dotted lines. The correspondence between these results and the original ε_{TL} is quite poor, especially below 10 eV and further down into the optical regime.

Relativistic Kramers-Kronig analysis

In order to extend the range of applications of the traditional KKA, it has been proposed to use the relativistic formulation as the underlying model for the calculation of the correction term [19]. This constitutes the framework for a relativistic KKA (rKKA), in which a new correction term, $S_c(E)$, contains all contributions except for the non-relativistic bulk term, $S_h^{ELF}(E) = S - S_c$ (see Eqs. 5 and 6).

Following these principles and with efficiency in mind, we implemented a rKKA using a modified DDCS, $D_c(\theta, E)$, calculated as;

$$D_c(\theta, E) = D(\theta, E) - D_b^{ELF}(\theta, E)$$
(7)

Where, $D_b^{ELF}(\theta,E)$ is the DDCS corresponding to the bulk semi-classical term S_b^{ELF} . Using this method, the correction can be calculated using a single numerical integration of the DDCS, which is desirable since this computation is costly.

These are the main ingredients for our rKKA implementation, and even in this basic form, the results are quite good, but not excellent. Fig. 1a shows the CDF retrieved after applying rKKA (dashed lines). The correspondence between these results and the original ε_{TL} is already much better than for the conventional KKA, reproducing the dielectric response down to the optical regime. Additionally, since the estimated S_c contains all relativistic contributions, it can be applied to the input spectrum to reveal S_b^{ELF} . This procedure is depicted in Fig. 1b, with the resulting spectra (dashed lines) showing good agreement with the theoretical $\Im(-1/\varepsilon_{TL})$.

However, the retrieved dielectric functions contain some ripples, obviously artefacts not observed in the original ε_{TL} models and the input S(E) spectra. Examining these spectra, it is clear that related errors have a more significant contribution near the band gap onset and at around 15 eV. Cerenkov and surface losses respectively impact these two regions, and the results indicate that the appearance of these ripples can be related to the incomplete suppression of these spurious contributions.

The origin of these issues, the effects of which can be observed in other similar works [23], is two-fold. Either the numerical integration is not completely reliable; or the initial guess of the CDF is too far from the ground truth; in this case, the original dielectric function. Gross errors are indeed apparent in the correction terms in the form of intense peaks that in turn produce negative intensity in some regions of the spectrum and high-frequency noise that can ultimately preclude the convergence of the algorithm.

In order to investigate and propose solutions to these issues, we analyze low-loss EELS synthetic data using our own rKKA algorithm that has been generated using also our own EELS simulation procedure. The computing time is also considered as hyperspectral acquisition methods are widespread and we can utilize this large amount of information to our advantage (see Section 3.3). Our aim is to be able to treat batches with many spectra at once, consequently efficient DDCS integration using several methods and parallel computation are investigated.

For this purpose, we use ε_{TL} models, with band gap energies between 1 and 6 eV, to calculate semi-classical and relativistic DDCS logmeshes. The parameters of the simulation are fixed to E_0 = 300keV, t=10-250nm and $\theta_{\rm max}$ =10mrad. Numerical integration of the logmeshes is optimized for speed and reliability, from $\theta_{\rm min}=0.1-1\mu{\rm rad}$, and an angular mesh size $N_\theta=256-512$. Poisson noise is added to the spectra used as input to the rKKA algorithm, to investigate also the effects of counting statistics. In this sense, simple tests indicate that to make the signal-to-noise (SNR) ratio drop appreciable for the spectra with low number of counts, a zero-loss intenstity of $I_0=1\cdot10^6~e^-$ is sufficient.

The rKKA algorithm is initialized using these spectra containing all

relativistic contributions. The normalization is performed using the thickness as a known parameter (refractive index normalization is also possible, but not used here). The rKKA loop runs until either convergence or a maximum of 20 iterations are reached. Convergence is indicated by the variation between iterations of the estimated relativistic correction, measured using a weighted test, $\chi^2(S_{s,i}, S_{s,i-1}) < 5 \cdot 10^{-4}$. The retrieved CDF and estimated ELF contributions can then be compared with the known ground truth counterparts; the original dielectric function and semi-classical spectrum.

3. Results

3.1. Optimization of the relativistic DDCS integration

We take into account several numerical integration methods (see Fig. 2a), running benchmark tests against the semi-classic dielectric model to test their reliability. Additionally, computational cost tests where performed measuring the average time spent in the calculation of a relativistic spectrum for datasets with sizes between 8 and 64 spectra (solid lines). In all cases, parallel processing was used on a workstation with 8 CPUs and 32 Gb of RAM.

The considered methods include Gaussian quadrature/cubature, Simpson rule and a log-sum-exp (LSE) trick integration. Gaussian quadrature integration is perhaps the most popular solution, already implemented in a freely available Matlab low-loss EELS simulation package [9]. Inspired on this solution, we have implemented a faster, multidimensional version using the freely available cubature Python wrapper [30–32]. The Simpson-rule method is based on the well-known numerical integration formula, generalized for irregularly-spaced data meshes. This method is implemented using the routine already available in the Hyperspy toolbox [24]. Finally, LSE trick is the more straightforward solution of summing the values in the log-mesh through the scattering angle dimension and performing the appropriate change of variables. This method is easily implemented based on the LSE routine available in the scipy package [33].

Our tests indicate that the Simpson-rule method gives a good balance between speed and reliability. It produces an optimum estimate and is the less time-consuming for medium size datasets, scoring between 0.25-0.14 s/spectrum for dataset sizes 4–64 spectra. In both this method and the LSE trick, and for larger datasets, the calculations benefit from cached operations meaning that the speed per spectrum increases. The LSE method is the less time-consuming method for larger datasets (below 0.13 s/spectrum), however, even if over/under-flow errors are taken into account it proves to be the less reliable. The errors are however small, and thus difficult to appreciate in Fig. 2a.

Finally, the cubature/quadrature methods are reliable but also more demanding, additionally requiring interpolation of the data prior to numerical integration. They are the most time-consuming, scoring 2 s/spectrum over all test sizes for the more efficient cubature method. Thus the cubature integration is not practical for performing fast batch calculations with many spectra. It is however useful to run tests when the DDCS angular mesh is being optimized.

The final version of our algorithm incorporates all the three featured methods, apart from the slower quadrature method (included for legacy reasons). Furthermore, routines for the prediction of the angular spread of radiative and non-radiative bulk inelastic scattering have also been incorporated. These are useful for the optimization of the DDCS logmeshes, and have been used together with the efficient Simpson-rule integration method for all the remaining calculations presented. For the results in this paper, log-meshes with 256 values and a $\theta_{\rm min}$ = 1µrad were considered. Using this optimized integration scheme, the simulation and rKKA processing of hyperspectral datasets with a few hundred spectra in a matter of minutes is possible.

3.2. Relativistic KKA of single spectra

In our preliminary results using a naive rKKA implementation (see Fig. 1), we observe rippling errors associated with the incomplete suppression of spurious contributions. Our investigation shows that these issues have a greater impact when surface-loss and Cerenkov-loss terms are relatively intense. Considering also the spectra in Fig. 2a, we observe that for the same thickness the impact of these contributions is greater when the ε_{TL} model with lower band gap energy is employed. The reason is that this model puts a greater oscillator strength into the absorption spectra, and consequently the spectral features are more pronounced. The physical equivalent would be a material that has a larger refractive index, for which the impact of radiative loss is naturally more important [28].

Ultimately, our implementation of the rKKA uses regularization of the correction term S_c by bounding and smoothing to improve the reliability of the iterative solutions. In this sense; bounding means that at each iteration the correction values at a given energy $S_c(E')$ are limited to a fixed percentage of the total intensity,

$$S_c^{bound}(E) = \begin{cases} S_c(E'), & S_c(E') < S(E')^* b_{KKA} \\ S_c(E') b_{KKA}, & \text{otherwise} \end{cases}$$
 (8)

where $b_{KKA} \in (0, 1)$ controls the bounding limits; e.g. $b_{KKA} = 1$ means that the correction can be exactly equal to the input signal but not greater. Following this procedure, the correction is smoothed using a Gaussian filter

$$S_c^{gauss}(E) = S_c^{bound} * G(\gamma_{KKA})$$
(9)

where the right-hand side denotes convolution with a Gaussian kernel, G, with an energy broadening parameter γ_{KKA} the value of which can be a few tens of eV.

This approach is equivalent to imposing previous knowledge about the intensity and shape of the correction term. In this sense, a $b_{KKA} < 1$ ensures that the intensity of S_c never surpasses the original S, introducing regions of negative spectral intensity in the input to the next iteration. Additionally, a moderate smoothing avoids the introduction of high-frequency oscillations which are not suppressed by the iterative reconstruction while preserving the relevant features of S_c .

The regularization procedures ensure that the calculated corrections converge and eliminates ripples in most cases. More precisely, for all the spectra that were simulated for specimen thicknesses above 40–50nm the $S_b^{ELF}(E)$ recovered by our rKKA are in excellent agreement with the original TL-DF and expected correction terms.

Fig. 4 showcases the correction results obtained using rKKA for thicknesses of 50 and 100 nm. These corrections are allowed to be almost as large as the input spectra by $b_{KKA} = 0.99$, and high-frequency oscillatory components above $\gamma_{KKA} = 0.2 \, \text{eV}$ are dampened. Examination of the spectra obtained after the application of these correction terms (dashed lines) confirms that the rippling features are largely removed.

On one hand, bulk effects (Cerenkov) can be robustly estimated using rKKA even when they are the main relativistic contribution to EELS, in thicker samples. Only the result obtained for 1eV band gap energy and 50nm thickness diverge noticeably from the expected bulk semi-classic contribution in the band gap energy onset region. In contrast, these issues are not affecting the result for t=100nm, although the intensity of Cerenkov-loss increases with thickness. The reason for this discrepancy has been identified to be the worse counting statistics for a thinner sample, a problem which is exacerbated in our synthetic datasets by the addition of Poisson noise.

On the other hand, surface effects represent the main source of artifacts in the solution. For relatively thin samples, gross errors are introduced that may be attenuated by bounding and smoothing, but can not be completely corrected using only the presented regularization methodology. It can be observed that these artefacts increase as the simulated thickness decreases (see Fig. 5, red lines). We determine that

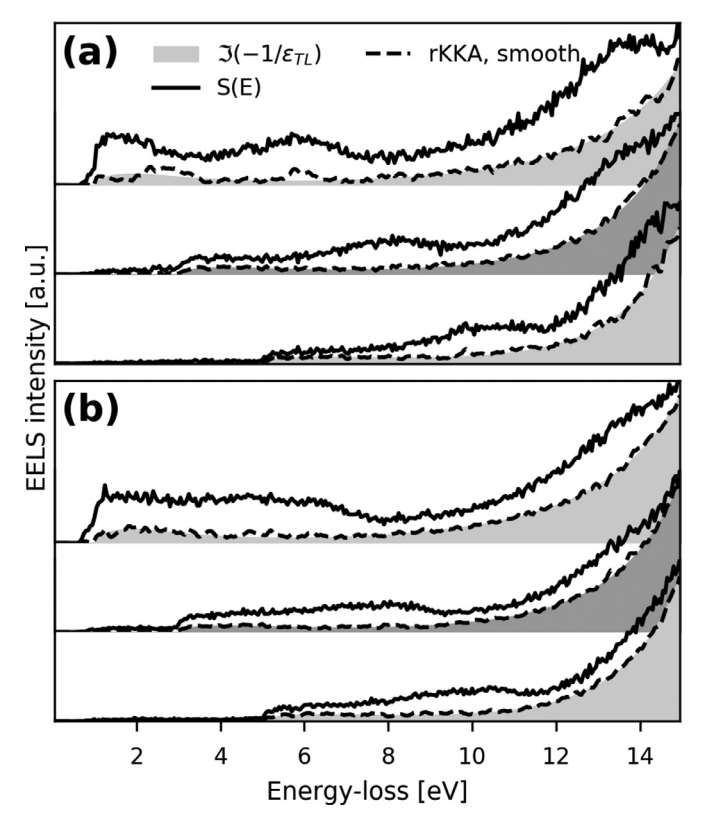


Fig. 4. For the same three ε_{TL} models presented in Fig. 1, panel (a) and (b) present regularized rKKA results for t=50 and 100 nm, respectively.

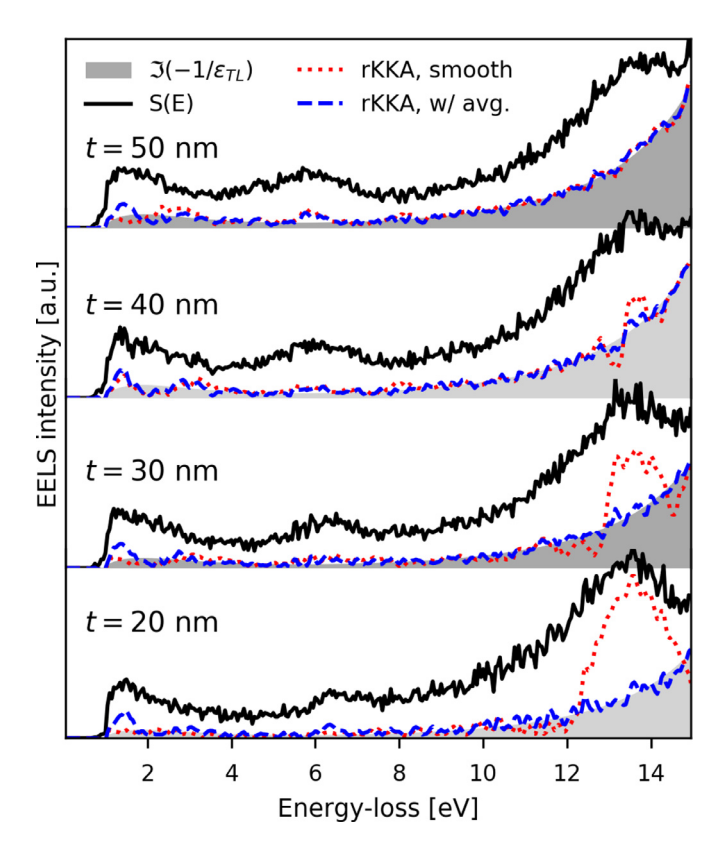


Fig. 5. For the same ε_{TL} models with $E_g = 1$ eV presented in Fig. 1, this figure presents regularized and average rKKA results for several thickness values, with red and blue dashed lines, respectively. Details of the simulation and analysis parameters are found in the text. (For interpretation of the references to colour in this figure legend, the reader is referred to the web version of this article.)

the origin of these issues is not the noise-response of the correction calculation, but the inadequacy of the initial guess for the CDF; see steps 2 and 3 in Fig. 3. In this sense, thinner regions have a larger relative contribution of surface losses. To eliminate the errors, it is important to improve the initial guess of the CDF, prior to the estimation of S_c . In the following section, we devise a methodology to do so, incorporating the information from hyperspectral datasets.

As a final note on the choice of bounding and smoothing parameters; we have noticed that the values described above work well in most cases. In an actual experiment, the smoothing can be adjusted depending on the energy resolution and/or point-spread function of the set-up. In case of doubt, preliminary rounds of a few iterations can be used to adjust these parameters. It is important to take into account that the choice if this parameters may affect the number of iterations employed to reach convergence can change. In extreme cases, bounding and smoothing the correction implies that the recovered may not converge to the original SSD; for instance in cases where the correction is above the selected percentage of the signal or the smoothing is so large that it removes relevant features from the correction.

3.3. Relativistic KKA of an EELS-SL

Hyperspectral acquisition modes, in which maps containing many spectra from areas of equal composition are acquired and analysed, is very common practice. For isotropic media, we can make the assumption that the only difference between spectra acquired from the same material region is the material thickness transversed by the electron beam. In this case, the dielectric properties causing the EELS are the same for each spectrum and can thus be described by a single $\varepsilon(E)$ function. We have replicated this situation in our simulations, generating a synthetic dataset equivalent to a hyperspectral line profile, commonly known as EELS spectrum-lines (SL). In this EELS-SL a linear thickness gradient exists between the spectra, and they are affected differently by spurious contributions; see Fig. 5, solid black lines.

Under the above assumption, it is therefore natural to use the same guess for the CDF to model each individual spectrum in our synthetic EELS-SL and calculate S_c . When this is done, the S and S_c in the EELS-SL are still different from one another, since they are calculated for their corresponding thickness. Considering this special case, we implement in our rKKA the possibility to average the CDF obtained for each spectrum in a hyperspectral dataset, ε_i^P , after application of the Kramers–Kronig transforms, to produce an average estimate,

$$\varepsilon_i^{\text{avg}}(E) = \frac{1}{N_p} \sum_{p=0}^{N_p} \varepsilon_i^p(E)$$
(10)

where p is an index for the spectra in the hyperspectral dataset, running from 0 to N_p . Note that in our implementation, ε_i^{avg} is only used for the calculation of S_c ; the single $\varepsilon_i^{\ p}$ corresponding to each point spectrum are stored and returned as a result after convergence or the last iteration are reached.

Fig. 5 depicts the results of this procedure when processing an EELS-SL with 21 spectra and a linear thickness gradient from 20 to 120nm. In this profile, the suppression of spurious contributions is good, and the corrected spectra are in excellent agreement with the expected bulk semi-classical contributions. Moreover, these average rKKA results and the results from single spectrum processing can be compared (see blue dashed and red dotted lines). The average rKKA produces a clearly more reliable reconstruction of the bulk semi-classical term. Most of the Cerenkov-loss signal at the band gap energy onset is correctly modelled and can be subtracted. Meanwhile, the strong rippling at around 15eV introduced by surface contributions disappears completely.

This average rKKA reconstruction is useful as long as it incorporates information from different single rKKA through the dataset in an advantageous way. It is possible to quantitatively assess the quality of the presented rKKA reconstructions, since the expected results are known

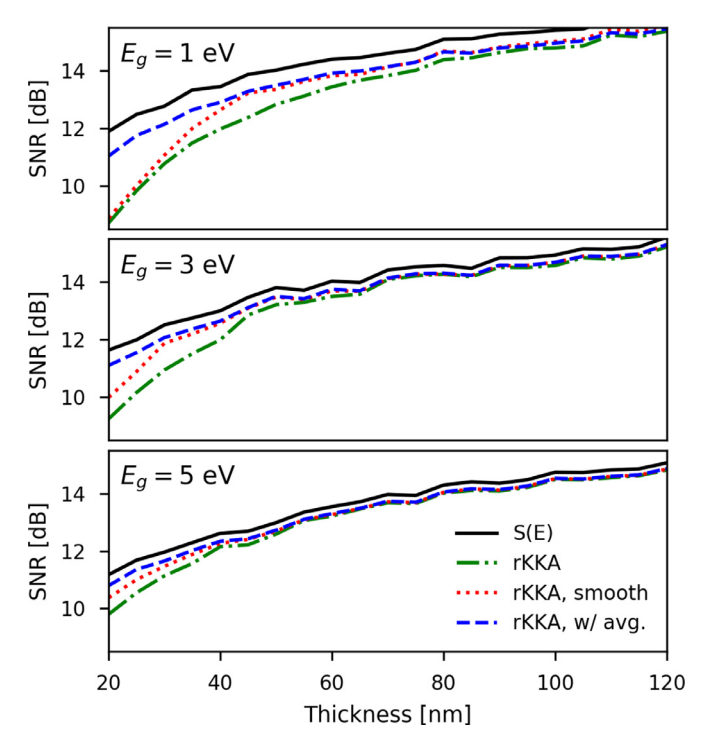


Fig. 6. From top to bottom, SNR measured using Eq. 11 for the rKKA reconstructions of the three ε_{TL} models in Fig. 1, in dashed lines. The rKKA is performed with the naive, regularized and average implementations; as indicated by green, red and blue colors, respectively. The SNR corresponding to the noisy spectra compared to the noise-less case is also included, in solid black lines. (For interpretation of the references to colour in this figure legend, the reader is referred to the web version of this article.)

beforehand. We perform this assessment on a logarithmic scale, using the following definition of SNR,

$$SNR = 10 \log_{10} \left(\frac{\int |S_b^{ELF}| dE}{\int |S - S_c - S_b^{ELF}| dE} \right)$$
 (11)

where, in the ratio, the denominator contains the integral of the expected semi-classical bulk contribution and the numerator contains the integral of the error for the obtained reconstruction of this contribution. Note that in this process the SNR of a spectrum is indicated by a single value, in dB. Figure 6 presents such assessment, where the expected and obtained bulk semi-classical contribution are compared for three different panels and through the whole EELS-SL (dashed lines). In the same figure, the quality of the noisy input S(E) is measured by comparing to the noise-less signal (solid lines). Since the quality of the input spectra is dominated by Poisson distributed noise, a linear decay is expected for SNR measured on a logarithmic scale.

Since our simulations are performed with fixed beam intensity and thicker specimens scatter strongly, an increase in the signal quality with thickness is expected. Indeed, the thickness dependence of the SNR for the noisy input signal is linear, showing a larger SNR than the reconstructions. The single rKKA reconstructions show a slight overall improvement when regularization is used, as rippling features are suppressed or attenuated. The average rKKA shows great improvement in the thinner region, especially for the lower band gap energy cases. In those cases, we have seen that the averaged results completely remove the spurious features caused by inadequacies in the CDF guesses. Also for the average rKKA at the lowest band gap (Eg $= 1~{\rm eV}$), the quality drops slightly in the thicker regions. Probably, the origin of this drop are strong features in thin regions not completely eliminated by the averaging.

We also explore the effect of using a shorter EELS-SL, that contains less spectra in the thicker regions by applying the average rKKA algorithm to two datasets; the first one, labeled A is a short EELS-SL with 21 spectra from 20 to 50nm (red dotted lines); dataset B, already presented above, has 21 spectra from 20 to 120nm (blue dashed lines).

Fig. 7 summarizes results obtained by this procedure at the 50nm thickness, which is the largest in dataset A. Again for the smaller band gap energy, the rippling features of the thinner regions have been introduced into the result for this thickness. The amount of spectra in this shorter EELS-SL in the thicker region is not sufficient to compensate for the errors introduced in the thinner regions.

Nevertheless, comparison of Figs. 1,4 and 5 shows that average rKKA results in all other cases are better than single rKKA results. Averaging adds to the robustness of the algorithm, given that a sufficient number of spectra are acquired from regions not critically impacted by spurious contributions (thinner or thicker).

3.4. Application to experimental data

We have also applied the rKKA algorithm to experimental EELS data of AlN, obtained from the EELS database open repository [34]. Fig. 8 includes the results from this procedure, showing the step-by-step treatment of EELS data to obtain the dielectric function. Panel (a) presents the treatment of the spectra prior to the application of the algorithm, including the careful deconvolution of the zero-loss peak (ZLP) and plural scattering. The ZLP model is obtained from the EELS data and a modified Voigt function to extend the part of the tail below the inelastic spectrum. In order to use the resulting SSD (dashed line) as an input for KKA, the high energy tail of the spectrum is extended smoothly to zero intensity using a power law [11]. Care was taken when applying these procedures to avoid artifacts. The examination of the resulting SSD (dashed line) shows that plural scattering is suppressed without modification of the main volume plasmon. The treatment allowed for the asymmetry of the ZLP tails which is a known feature of spectra acquired using a field-emission gun (FEG) [35,36].

Since this spectrum was acquired using a 200 kV high-tension beam, the resulting SSD contains a strong contribution of relativistic electrons affecting the band gap region (~ 6.3 eV, for AlN). Fig. 8 (b) shows the removal of the relativistic contribution calculated using rKKA. For this calculation the smoothing parameter was set to 1 eV, corresponding to the observed ZLP width. The rKKA loop ran until $\chi^2 < 10^{-4}$ convergence was reached. The resulting ELF spectrum (dashed line) has its intensity onset at ~ 6.3 eV, in good agreement with the expected value for the AlN band gap and measurements by other authors [37]. Our ability to determine the precision of this observation is limited by the coarse energy-loss sampling of this spectrum (0.1 eV), but it is presumably not smaller than 0.8 eV since a Schottky-FEG source was employed. The measurement can be improved by employing a monochromated source, finer energy-loss sampling and possibly a larger detector.

Fig. 8 (c) shows that the agreement of the dielectric function obtained using rKKA also improves, if we compare with theoretical results from DFT calculations. In this figure, the imaginary part of the dielectric function is shown, which shows band-structure transitions related with the optical oscillator strength. In the case of the experimental EELS results, spectral broadening and the presence of collective excitation (bulk plasmon), could explain the different peaks and slightly more intense high-energy tail observed, respectively. Nevertheless, the overall agreement for the rKKA result and DFT simulation is excellent.

4. Conclusion

In the case that a relativistic contribution to EELS cannot be disregarded traditional KKA does not guarantee retrieving the correct CDF, even from perfect noise-less input data. In turn, rKKA allows to retrieve the correct CDF and a meaningful correction term, even in a relatively naive implementation. However, in order to use low-loss EELS for standard-free measurement of the dielectric properties of a material,

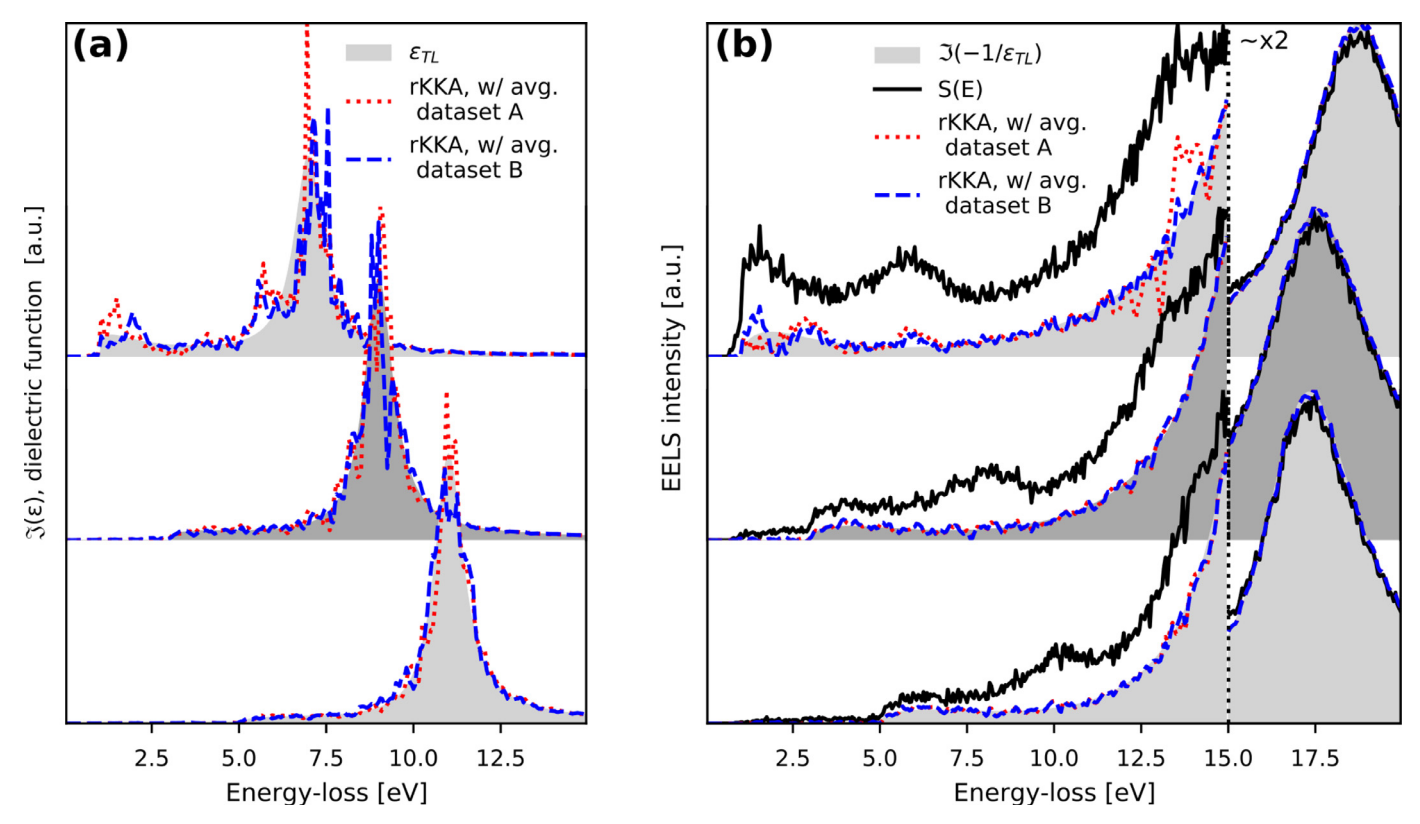


Fig. 7. Comparison of the ε_{TL} model simulations and average rKKA results for t=50 nm and $E_g=1$, 3, 5 eV, from top to bottom (see Fig. 1). Panel (a) shows the imaginary part of the models (grey areas) compared to average rKKA reconstructions obtained using datasets A and B as per explained in the text (red and blue dashed lines, respectively). Panel (b) shows the $\Im(-1/\varepsilon)$ contribution (grey areas) and the relativistic spectra (solid lines) calculated for these models. Two dashed lines shows the estimated $\Im(-1/\varepsilon)$ contribution for datasets A and B, again in red and blue color, respectively. (For interpretation of the references to colour in this figure legend, the reader is referred to the web version of this article.)

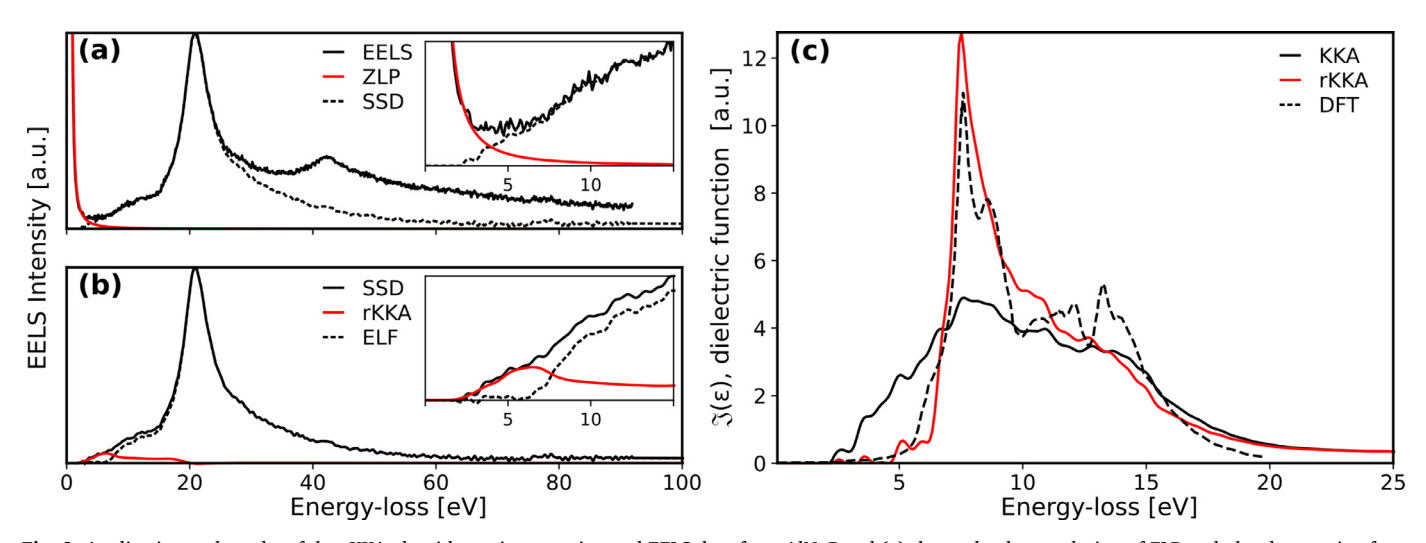


Fig. 8. Application and results of the rKKA algorithm using experimental EELS data from AlN. Panel (a) shows the deconvolution of ZLP and plural scattering from the raw EELS (solid black line) using a ZLP model (red line). Panel (b) shows the deconvolution of relativistic effects from the SSD (solid black line) using the relativistic correction obtained by rKKA (red line). Panel (c) shows the dielectric function obtained using classic and relativistic KKA algorithms, in solid black and red lines, respectively. These experimental results are compared with theoretical results from DFT simulations [38]. (For interpretation of the references to colour in this figure legend, the reader is referred to the web version of this article.)

the speed and reliability of the rKKA present challenging issues. In this paper, we have explored and proposed solutions to these issues.

The time-consuming and error prone computation of relativistic spectra is one of the main issues. According to our calculations, an optimized numerical integration scheme using the Simpson-rule improves the speed of the DDCS integration by one order of magnitude. This feat additionally allows batch processing of hyperspectral datasets,

which becomes relevant when analyzing noisy experimental data.

The results from the naive implementation of rKKA are plagued by artifacts, related to the inaccuracy of the initial guess for the CDF and the noise-response of the DDCS integration. When treated using simple regularization by bounding and smoothing, we have shown, that these errors can be suppressed or at least severely attenuated. This methodology makes rKKA more robust in the majority of cases. However, in

very thin samples regularization by itself is insufficient, and some errors always remain. We have proposed to use batch analysis of hyperspectral datasets, showing how averaging of the CDF improves the performance of rKKA. This improvement is confirmed using SNR measurements as a validation figure. We foresee that this simple averaging trick could be improved in the future by thickness-dependent weighting of the information from different energy-loss regions.

The present study broadens the application range of KKA to situations in which relativistic and surface losses have larger impact in the spectra than ever before. Some limitations of the technique remain, the application of KKA to very thin or thick specimens still remains problematic because of the inadequacy of the normalization procedure and the effect of beam broadening.

Acknowledgments

Funded by the Deutshe Forschungsgemeinschaft (DFG) – Projectnummer 182087777 – SFB951.

References

- C. Hébert, Practical aspects of running the WIEN2k code for electron spectroscopy, Micron 38 (1) (2007) 12–28.
- [2] V.J. Keast, An introduction to the calculation of valence EELS: quantum mechanical methods for bulk solids, Micron 44 (2013) 93–100.
- [3] A. Eljarrat, X. Sastre, F. Peiró, S. Estradé, Density functional theory modeling of low-loss electron energy-loss spectroscopy in wurtzite iii-nitride ternary alloys, Microsc. Microanal. 22 (3) (2016) 706–716.
- [4] P. Yu, M. Cardona, Fundamentals of Semiconductors: Physics and Materials Properties, Graduate Texts in Physics, Springer, 2010.
- [5] A. Eljarrat, S. Estradé, v. Gačević, S. Fernández Garrido, E. Calleja, C. Magén, F. Peiró, Optoelectronic properties of inaln/GaN distributed bragg reflector heterostructure examined by valence electron energy loss spectroscopy, Microsc. Microanal. 18 (2012) 1143–1154, https://doi.org/10.1017/S1431927612001328.
- [6] A. Eljarrat, L. López-Conesa, J. López-Vidrier, S. Hernández, B. Garrido, C. Magén, F. Peiró, S. Estradé, Retrieving the electronic properties of silicon nanocrystals embedded in a dielectric matrix by low-loss EELS, Nanoscale 6 (24) (2014) 14071–14083
- [7] J. Daniels, C.v. Festenberg, H. Raether, K. Zeppenfeld, Optical constants of solids by electron spectroscopy, Springer Tracts in Modern Physics, Volume 54, Springer, 1970, pp. 77–135.
- [8] H. Raether, Excitation of Plasmons and Interband Transitions by Electrons, Springer, 1980.
- [9] R.F. Egerton, Electron Energy-Loss Spectroscopy in the Electron Microscope, 3rd, Springer US, 2011.
- [10] R.H. Ritchie, Plasma losses by fast electrons in thin films, Phys. Rev. 106 (5) (1957) 874.
- [11] A. Eljarrat, S. Estradé, F. Peiró, Quantitative methods for electron energy loss spectroscopy, in: P. Hawkes (Ed.), Advances in Electron Imaging and Physics, 2090 Elsevier, 2018. In press
- [12] E. Kröger, Berechnung der energieverluste schneller elektronen in dünnen schichten mit retardierung, Zeitschrift für Physik 216 (2) (1968) 115–135.
- [13] C.v. Festenberg, E. Kröger, Retardation effects for the electron energy loss probability in gap and si, Phys. Lett. A 26 (8) (1968) 339–340, https://doi.org/10.1016/0375-9601(68)90360-5.
- [14] W. Zhan, V. Venkatachalapathy, T. Aarholt, A.Y. Kuznetsov, Ø. Prytz, Band gap maps beyond the delocalization limit: correlation between optical band gaps and plasmon energies at the nanoscale, Sci. Rep. 8 (848) (2018) 2045–2322.
- [15] M. Stöger-Pollach, H. Franco, P. Schattschneider, S. Lazar, B. Schaffer, W. Grogger,

- H. Zandbergen, Čerenkov losses: a limit for bandgap determination and Kramers–Kronig analysis, Micron 37 (5) (2006) 396–402.
- [16] R. Erni, N.D. Browning, The impact of surface and retardation losses on valence electron energy-loss spectroscopy, Ultramicroscopy 108 (2) (2008) 84–99.
- [17] L. Gu, V. Srot, W. Sigle, C. Koch, P. van Aken, F. Scholz, S.B. Thapa, C. Kirchner, M. Jetter, M. Rühle, Band-gap measurements of direct and indirect semiconductors using monochromated electrons, Phys. Rev. B 75 (2007) 195214, https://doi.org/10.1103/PhysRevB.75.195214.
- [18] M. Stöger-Pollach, Optical properties and bandgaps from low loss EELS: pitfalls and solutions, Micron 39 (8) (2008) 1092–1110.
- [19] M. Stöger-Pollach, A. Laister, P. Schattschneider, Treating retardation effects in valence eels spectra for kramers-kronig analysis, Ultramicroscopy 108 (5) (2008) 439-444
- [20] L. Gu, W. Sigle, C.T. Koch, J. Nelayah, V. Srot, P.A. van Aken, Mapping of valence energy losses via energy-filtered annular dark-field scanning transmission electron microscopy, Ultramicroscopy 109 (2009) 1164–1170, https://doi.org/10.1016/j. ultramic 2009 05 001
- [21] L. Zhang, R. Erni, J. Verbeeck, G. Van Tendeloo, Retrieving the dielectric function of diamond from valence electron energy-loss spectroscopy, Phys. Rev. B 77 (19) (2008) 195119
- [22] K. Mkhoyan, T. Babinec, S. Maccagnano, E. Kirkland, J. Silcox, Separation of bulk and surface-losses in low-loss eels measurements in stem, Ultramicroscopy 107 (4–5) (2007) 345–355.
- [23] Q. Meng, L. Wu, H.L. Xin, Y. Zhu, Retrieving the energy-loss function from valence electron energy-loss spectrum: Separation of bulk-, surface-losses and cherenkov radiation, Ultramicroscopy 194 (2018) 175–181.
- [24] F. de la Peña et al., hyperspy/hyperspy v1.4.1 (2018). 10.5281/zenodo.1469364.
- [25] A. Eljarrat, Relativistic eels code repository, 2018, (https://github.com/AEljarrat/relativistic_eels).
- [26] J. Lindhard, On the properties of a gas of charged particles, Kgl. Danske Videnskab. Selskab Mat.-Fys. Medd., 1954 Ph.D. thesis.
- [27] G. Jellison Jr, Spectroscopic ellipsometry data analysis: measured versus calculated quantities, Thin Solid Films 313 (1998) 33–39.
- [28] F.J. García de Abajo, Optical excitations in electron microscopy, Rev. Modern Phys. 82 (2010) 209–275, https://doi.org/10.1103/RevModPhys.82.209.
- [29] D.W. Johnson, A fourier series method for numerical kramers-kronig analysis, J. Phys. A 8 (4) (1975) 490.
- [30] S.G. Castro, C. Mittelstedt, F.A. Monteiro, R. Degenhardt, G. Ziegmann, Evaluation of non-linear buckling loads of geometrically imperfect composite cylinders and cones with the ritz method, Compos. Struct. 122 (2015) 284–299.
- [31] S.G. Castro, C. Mittelstedt, F.A. Monteiro, M.A. Arbelo, R. Degenhardt, G. Ziegmann, A semi-analytical approach for linear and non-linear analysis of unstiffened laminated composite cylinders and cones under axial, torsion and pressure loads, Thin-Walled Struct. 90 (2015) 61–73.
- [32] S. Castro, A. Loukianov, Python wrapper for cubature: adaptive multidimensional integration, 2017, Version 0.13.3.
- [33] E. Jones, T. Oliphant, P. Peterson, et al., SciPy: Open source scientific tools for Python, 2018.
- [34] P. Ewels, T. Sikora, V. Serin, C.P. Ewels, L. Lajaunie, A complete overhaul of the electron energy-loss spectroscopy and x-ray absorption spectroscopy database: eelsdb.eu, Microsc. Microanal. FirstView (2016) 1–8, https://doi.org/10.1017/ S1431927616000179.
- [35] R. Erni, N.D. Browning, Valence electron energy-loss spectroscopy in monochromated scanning transmission electron microscopy, Ultramicroscopy 104 (2005) 176–192
- [36] T. Walther, H. Stegmann, Preliminary results from the first monochromated and aberration corrected 200-kv field-emission scanning transmission electron microscope, Microsc. Microanal. 12 (2006) 498–505.
- [37] H. Amari, H.Y. Zhang, L. Geelhaar, C. Chèze, M.J. Kappers, T. Walther, Nanoscale EELS analysis of elemental distribution and band-gap properties in AlGaN epitaxial layers, Journal of Physics: Conference Series, 326 IOP Publishing, 2011, p. 012039.
- [38] L.X. Benedict, T. Wethkamp, K. Wilmers, C. Cobet, N. Esser, E.L. Shirley, W. Richter, M. Cardona, Dielectric function of wurtzite GaN and AlN thin films, Solid State Commun. 112 (3) (1999) 129–133, https://doi.org/10.1016/S0038-1098(99) 00323-3.